Phase diagram of the orthorhombic, lightly lutetium doped $EuMnO_3$ magnetoelectric system

J. Oliveira,[1] J. Agostinho Moreira,[1,*] A. Almeida,[1] M. R. Chaves,[1] J. M. M. da Silva,[1] J. B. Oliveira,[1] M. A. Sá,[1] P. B. Tavares,[2] R. Ranjith,[3] and W. Prellier[3]

[1]*IFIMUP and IN-Institute of Nanoscience and Nanotechnology, Departamento de Física e Astronomia da Faculdade de Ciências, Universidade do Porto, Rua do Campo Alegre, 687, 4169-007 Porto, Portugal.*

[2]*Centro de Química. Universidade de Trás-os-Montes e Alto Douro, Apartado 1013, 5001-801. Vila Real, Portugal.*

[3]*Laboratoire CRISMAT, CNRS UMR 6508, ENSICAEN, 6 Boulevard du Maréchal Juin, F-14050 Caen Cedex, France.*

(Received 31 May 2011; published 15 September 2011)

This paper reports on structural, magnetic, dielectric, thermodynamic, and magnetodielectric properties of $Eu_{1-x}Lu_xMnO_3$, with $0 \leqslant x \leqslant 0.2$, towards the ($x$, T) phase diagram. The phase diagram reflects the effect of lattice distortions induced by the isovalent substitution of Eu^{3+} by smaller Lu^{3+} ions, which gradually unbalances the antiferromagnetic against the ferromagnetic exchange interactions, enabling the emergence of both ferroelectricity and magnetoelectric coupling. For $x < 0.1$, the paramagnetic phase is followed by a presumably incommensurate collinear antiferromagnetic phase AFM-1, and then a weak ferromagnetic phase seems to be established, with a canted A-type antiferromagnetic order. For $0.1 \leqslant x \leqslant 0.2$, the AFM-1 phase is followed by an antiferromagnetic phase AFM-2 with modulated spiral spin arrangement, compatible with ferroelectricity. The disappearance of hysteresis cycles $P(E)$ at low temperatures, clearly indicates the existence of an antiferromagnetic phase AFM-3, whose spin structure is not compatible with both the ferroelectric and ferromagnetic components. The magnetic behavior of $EuMnO_3$ and $Eu_{0.9}Lu_{0.1}MnO_3$ suggests the existence of a phase line separating the AFM-1 phase from the AFM-2 and AFM-3 phases, which is observed for $x = 0.1$. Magnetodielectric coupling was evidenced for both $x = 0.1$ and 0.2 compositions. Ferroelectric polarization and magnetodielectric coupling coefficient are larger for the latter composition.

DOI: 10.1103/PhysRevB.84.094414 PACS number(s): 75.47.Lx, 75.85.+t, 75.30.Kz, 77.80.B−

I. INTRODUCTION

Transition metal oxides are an interesting field of research in condensed matter physics due their unique wide range of physical properties. Among the transition metal oxides, rare-earth manganites have attracted the interest of the scientific community because some of them exhibit magnetoelectric coupling, being thus appealing materials for fundamental physics and for applications, namely their use as barriers and interfaces in electrically controlled spin transport.[1–4]

Although there are a large number of studies regarding the microscopic mechanisms underlying the magnetoelectric coupling, a universal theoretical approach is not achieved yet. For some magnetoelectric materials, it has been proposed that ferroelectricity is originated from a variety of modulated magnetic structures and can be explained in terms of the inverse Dzyaloshinskii–Moriya model.[5–10] On the grounds of this model, the interaction between spins, arranged in a modulated structure, deforms the crystal lattice, yielding the loss of the spatial inversion center and, thus, enabling the emergence of an electric polarization. As the electric polarization arises from lattice distortions, the study of the coupling between spins and phonons is of most relevance in these systems, wherein magnetic and ferroelectric properties are coupled. Consequently, from both fundamental and application points of view, a deeper understanding of magnetoelectric coupling in a large set of compounds remains a very important issue, namely the interplay between crystal structure and magnetic exchange interactions leading the magnetoelectric properties.

The most studied magnetoelectric materials are the orthorhombic rare-earth manganites, such as $EuMnO_3$, $GdMnO_3$, $TbMnO_3$, and $DyMnO_3$.[11–17] These systems exhibit rather interesting phase diagrams with magnetically driven ferroelectric phases for compounds with the lighter rare-earth ions or magnetically switching of electric polarization for those ones with the heavier rare-earth ions.[9] These materials behave differently since, by changing rare-earth ion size, the Mn-O1-Mn bond angle changes accordingly, and hence, the balance between ferromagnetic and antiferromagnetic interactions, in agreement with the model developed by Mochizuki and Furukawa.[10] Unfortunately, the change of rare-earth ions also brings changes to the magnetic state through its own magnetic characteristics. In order to understand the ion radius size effect, the solid solutions obtained by A-site substitution in europium manganite with a nonmagnetic ion with a smaller radius than europium will ensure the aforesaid requisites. Up to now, the Y-doped $EuMnO_3$ system, in which neither yttrium nor europium ions possess magnetic moment, has been extensively studied in both theoretical and experimental approaches.[18–25] In this system, the magnetic moments stem only from the Mn^{3+} ions, and both crystal and magnetic structures are strongly dependent on the Y concentration. As a consequence, this system exhibits rather interesting (x, T) and (B, T) phase diagrams, which have been explained in the framework of the Mochizuki and Furukawa model.[10,18–20,26]

Following this conceptual framework, we processed Lu-doped $EuMnO_3$, wherein the magnetic moments arise from the Mn^{3+} spins. We have chosen the end member of the lanthanide series, as it presents the smallest ionic radius. Hence, we expect that the partial substitution of Eu^{3+} by Lu^{3+} enhances the crystal deformations without altering the magnetic structure and, consequently, the unbalance between the antiferromagnetic and ferromagnetic exchange interactions underlying the magnetoelectric coupling. In this paper, we report an experimental study of the crystal structure of

$Eu_{1-x}Lu_xMnO_3$, with $0 \leqslant x \leqslant 0.2$ at room temperature, as well as, the magnetic, dielectric, ferroelectric, thermodynamic, and magnetodielectric properties of this system at low temperatures, in order to fully characterize its (x, T) phase diagram.

II. EXPERIMENTAL DETAILS

The samples studied in this work were prepared by a sol-gel combustion method, and they were characterized in terms of chemical, morphological, and microstructure by using powder X-ray diffractometry, scanning electron microscopy, and X-ray photoemission spectroscopy techniques. Details of sample processing are available in Ref. 27.

The heat capacity was measured in an ARS Cryocooler, between 8 and 300 K, in a quasi-adiabatic fashion by means of an impulse heating technique.

The samples used to perform the dielectric and polar measurements have the form of a regular parallelepiped. Gold electrodes were deposited using the evaporation method. The complex dielectric constant was measured with an HP4284A impedance analyzer, in the 8–300 K temperature range, under an ac electric field of amplitude 1 V/cm for 10 KHz and 1 MHz. The $P(E)$ relations were recorded between 8 and 50 K using a modified Sawyer–Tower circuit. In order to prevent any dynamical response from masking the actual domain reversal, we chose to perform the measurements of the $P(E)$ at enough low-operating frequencies. As the $P(E)$ relations do not change with frequency below 1 Hz, we have taken 330 mHz as the operating frequency. The $P(E)$ curves were measured by changing the temperature in small steps, namely in the ferroelectric phases where a 0.3 K step was chosen, in order to follow in detail any changes on both remanent polarization and coercive electric field. The electric voltage maximum applied to the sample was 1,000 V. On this regard, the corresponding electric field maximum amplitude is large enough to induce the full orientation of the ferroelectric domains. The sensibility of the electric polarization measurements is 2 $\mu C/m^2$.

Low-field dc-induced specific magnetization measurements were carried out using commercial superconducting quantum interference device (SQUID) magnetometer in the temperature range 4–300 K. The measuring magnetic field strength was 40 Oe.

The measurements of the magnetic field dependence of the dielectric constant were carried out using a PPMS Quantum Design cryostat. The capacitance was measured using an Agilent 4248A RLC bridge at different frequencies.

III. EXPERIMENTAL RESULTS AND DISCUSSION

A. Chemical and morphological characterization

The valence of europium ion in $Eu_{1-x}Lu_xMnO_3$ was checked by X-ray photoemission spectroscopy, and only the valence +3 (Eu^{3+}) was detected.

The technique used for the sample processing involves the rapid cooling of the samples from 1,350 °C to room temperature in about 15 min. According to Ref. 28, this procedure of sample preparation ensures the stoichiometry of oxygen according to the chemical structure $Eu_{1-x}Lu_xMnO_3$. Therefore, and since the concentration of oxygen deficiencies are not significant, it is possible to conclude that the valence of the manganese ion is +3 (Mn^{3+}).

The morphology and microstructure of the samples were determined with scanning electron microscopy. The ceramic samples exhibit a typical microstructure with high compactness and regular grain size and shape. The average grain size is 5 μm.

B. Crystal structure at room temperature

Figure 1 shows the X-ray powder diffraction spectra obtained for $Eu_{1-x}Lu_xMnO_3$ at room temperature with x = 0, 0.1, 0.2, 0.3, 0.4, 0.6, 0.8, and 1.

The average density of the samples, calculated from the data obtained with the X-ray diffraction technique, is 7.056 ± 0.001 g.cm^{-3}, whereas the average density determined experimentally from the ratio of the experimental value of the mass of the sample and its volume is 6.941 ± 0.005 g.cm^{-3}, which enables one to conclude that the degree of compaction of the samples is 98%.

The X-ray powder diffraction spectrum of $EuMnO_3$ exhibits the typical *Pbnm* orthorhombic structure.[29] Despite small shifts due to different unit cell dimensions, the samples with lutetium concentrations $x = 0.1$ and 0.2 exhibit similar X-ray powder diffraction patterns as undoped $EuMnO_3$. This means that these compounds have the same *Pbnm* orthorhombic

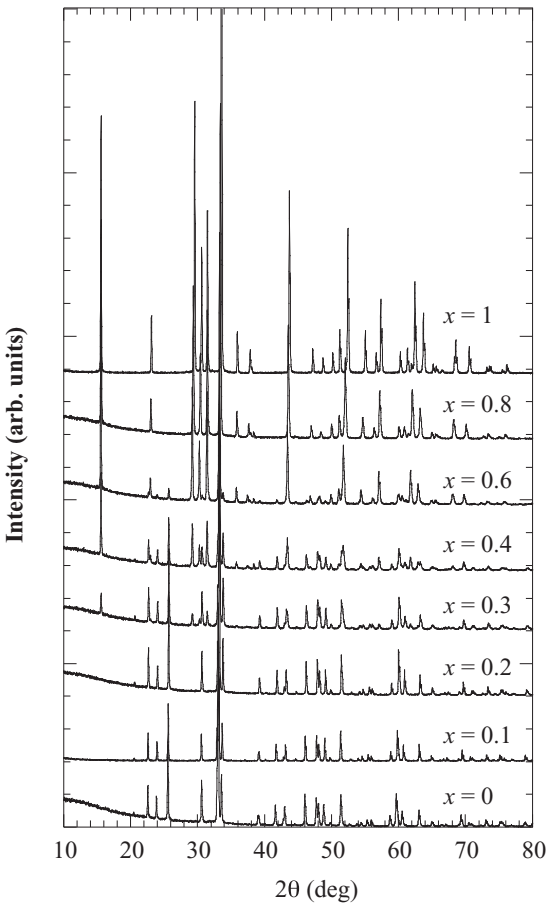

FIG. 1. X-ray powder diffraction spectra obtained for $x = 0$, 0.1, 0.2, 0.3, 0.4, 0.6, 0.8, and 1, recorded at room temperature.

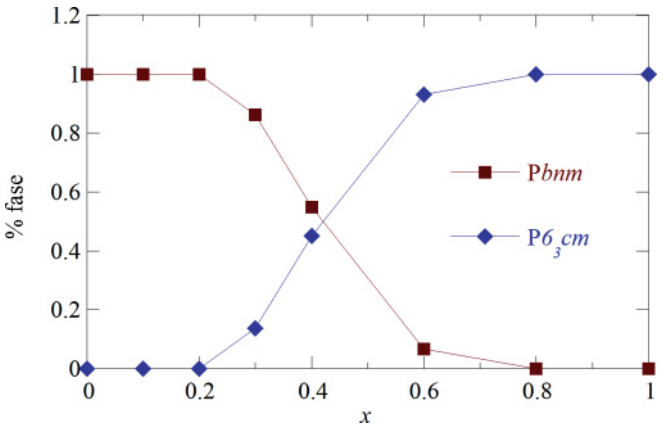

FIG. 2. (Color online) Molar percentage of orthorhombic *Pbnm* and hexagonal $P6_3cm$ phases as a function of Lu^{3+} concentration.

structure. On the other hand, the X-ray pattern of the $YMnO_3$ is compatible with the hexagonal structure $P6_3cm$, as reported for single crystals.[30] The compound with $x = 0.8$ exhibits similar X-ray spectrum as $YMnO_3$, evidencing the same hexagonal structure. No secondary phases could be observed for the compounds with $0 \leqslant x \leqslant 0.2$ and $0.8 \leqslant x \leqslant 1$. However, for the concentration range $0.3 \leqslant x \leqslant 0.6$, the X-ray spectra clearly show Bragg peaks coming from both orthorhombic and hexagonal structures. Figure 2 shows the molar percentage of orthorhombic and hexagonal phases as a function of x, obtained from the analysis of the X-ray spectra shown in Fig. 1. As the Lu^{3+} concentration increases from 0.3 towards 0.6, the molar percentage of the *Pbnm* phase decreases, while the molar percentage of hexagonal $P6_3cm$ phase increases. For the concentration $x = 0.4$, almost 50% of both phases are found. This result shows that the chemical route followed in this paper did not enable us to obtain single-phase samples with Lu^{3+} content between $0.3 \leqslant x \leqslant 0.6$.

In the following, we will only present the experimental results concerning the orthorhombic samples ($0 \leqslant x \leqslant 0.2$).

The crystal structure at room temperature was refined by using the Rietveld method. Figure 3 shows an example of the experimental data, the calculated X-ray pattern, and the difference between these two spectra for the $Eu_{0.9}Lu_{0.1}MnO_3$ compound. The structures of the unit cell of the three studied compositions are similar, having $Z = 4$. Figure 4 shows the *ab* and *bc* projections of the unit cell of $Eu_{0.9}Lu_{0.1}MnO_3$ at room temperature. The crystal structure is described as a network of corner-sharing tilted MnO_6 octahedra, forming chains along the *c* axis, which is typical for the family of rotationally distorted perovskites. The Eu^{3+} and Lu^{3+} ions occupy the interstices between the octahedra (*A* site).

1. Lattice parameters and structural deformations

Figure 5(a) shows the lattice parameters and cell volume as a function of Lu^{3+} concentration. The lattice parameters well satisfy the relation $c/\sqrt{2} < a < b$, which has been typically found in several rare-earth manganites presenting distortions of the octahedral environment of the Mn^{3+} ions, due to the Jahn–Teller distortion of the MnO_6 units.[31] The substitution of Eu^{3+} by the smaller ionic radius Lu^{3+} leads to a decrease of the lattice parameters and, consequently, of the cell volume. This fact is apparently associated with the decrease of the effective *A* site size. The slope of the $b(x)$ ($\frac{\Delta b}{\Delta x} = -0.071 \pm 0.005$ Å) is smaller than the ones of the $a(x)$ and $c(x)$, which are quite similar ($\frac{\Delta a}{\Delta x} \approx \frac{\Delta c}{\Delta x} = -0.12 \pm 0.02$ Å). This kind of behavior is observed also in other rare-earth manganites, and it has been attributed to the tilting of the MnO_6 octahedra, for which the distortion driven by a reduction of the *A*-site effective size leaves *b* slightly *x* dependent.

The aforementioned decrease of unit cell volume as the Lu^{3+} concentration increases is a direct consequence of the decrease of both *A*-site effective size and the Mn-O1-Mn bond angle, as it will be discussed later. Figure 5(c) shows the unit

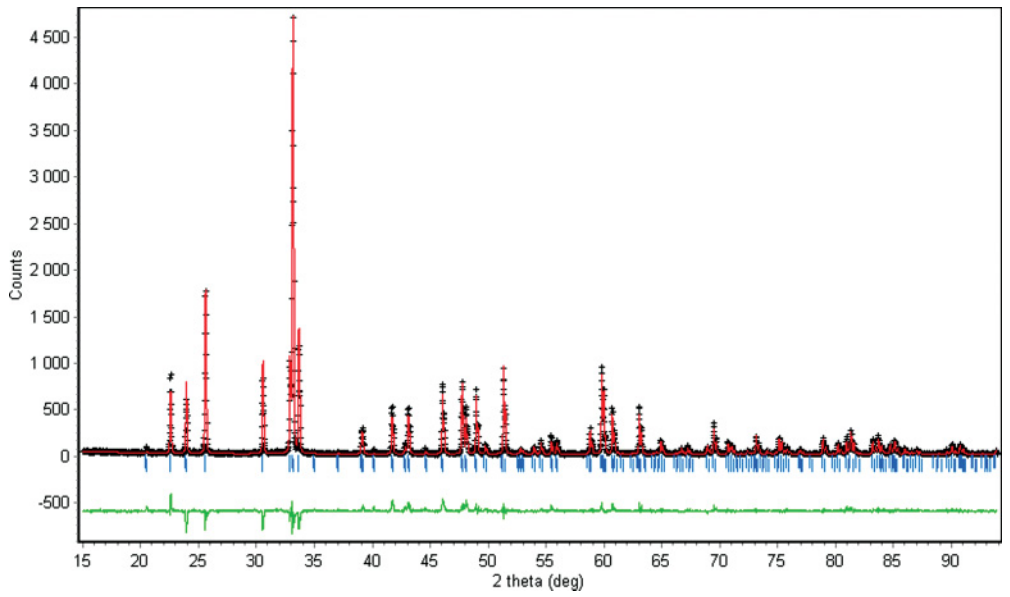

FIG. 3. (Color online) Observed, calculated and difference X-ray diffraction patterns for the $Eu_{0.9}Lu_{0.1}MnO_3$ at room temperature.

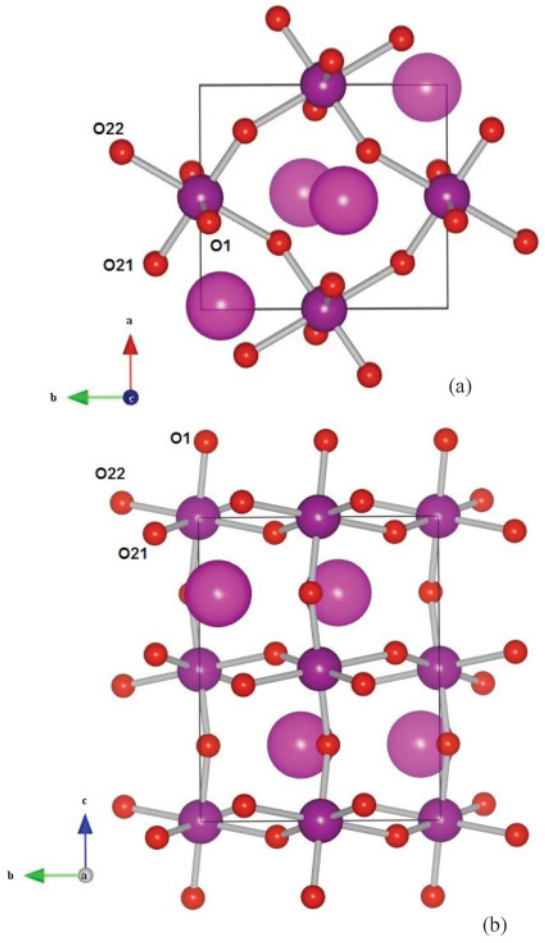

FIG. 4. (Color online) (a) *ab* and (b) *bc* projections of the unit cell of $Eu_{0.9}Lu_{0.1}MnO_3$ at room temperature.

cell volume as a function of the cube of the *A*-site effective size, defined as:

$$r_A = (1-x)r_{\mathrm{Eu}}^{12} + xr_{\mathrm{Lu}}^{12}. \quad (1)$$

In Eq. (1) $r_{\mathrm{Eu}}^{12} = 1.29\,\text{Å}$ and $r_{\mathrm{Lu}}^{12} = 1.20\,\text{Å}$ are the ionic radius of Eu^{3+} and Lu^{3+} ions for the coordination 12, respectively. These values were calculated from the data presented in Ref. 32. From Fig. 5(c), we conclude that the unit cell volume scales rather well with the *A*-site effective volume. It is worth stressing that the decreasing in the unit cell volume strongly influences the magnetic exchange interactions through the electronic orbital overlapping and, in this way, the magnetic properties of these materials, as it has been observed in other rare-earth manganites.[8,10]

In order to characterize the deformation of the lattice in relation to the ideal cubic symmetry, other parameters were calculated. One is the spontaneous orthorhombic strain, which is defined by the expression:[28]

$$e = \frac{2(b-a)}{b+a}, \quad (2)$$

where a and b denote the values of two lattice parameters. Figure 5(b) shows the spontaneous orthorhombic strain parameter e as a function of x. As it can be seen, the value of $e(x)$ increases monotonically with the concentration of Lu^{3+}, corroborating the increasing deformation of the lattice with respect to the ideal cubic structure. The increase of the spontaneous orthorhombic strain suggests a continuous octahedra tilting, which leads to changes in the lattice parameters, and significant variation in the Mn-O1-Mn bond angle. The deformation in relation to the ideal cubic perovskite structure can also be quantified by the tolerance factor t, introduced by Goldschmidt:[33]

$$t = \frac{r_A + r_O}{\sqrt{2}(r_B + r_O)}, \quad (3)$$

where r_A and r_B are the ionic radii of ions present on *A* site and *B* site, considering the coordination 12 and coordination 6, respectively, and r_O is the ionic radius of O^{2-}. In this case, $r_B = r_{\mathrm{Mn}}^{6} = 0.72\,\text{Å}$.[32] Figure 5(b) shows the tolerance factor as a function of x. As the Lu^{3+} concentration increases, the value of the tolerance factor decreases, deviating from its ideal value.

2. *Bond lengths and bond angle*

The Rietveld refinement procedure enables us to determine the atomic positions, from which we have calculated the bond lengths and bond angles involved in the MnO_6 octahedra. Among these, particular attention was given to the Mn-O bond length and Mn-O1-Mn bond angle, whose x dependence is shown in Figs. 5(d) and 5(e), respectively.

Significant distortions in the MnO_6 units were revealed from the analysis of the Mn-O bond lengths. We have found three different values for the Mn-O bond lengths for each composition, as it is shown in Fig. 5(d). While only one value for the Mn-O1 bond length is obtained, two different values were determined for the Mn-O2 bond length in the equatorial plane of the MnO_6 octahedron. The Mn-O bond lengths are quite independent on the Lu^{3+} concentration, and the average difference between the largest and smallest Mn-O2 bond lengths is about 0.28 Å. The difference between the Mn-O2 bond lengths is a direct consequence of the Jahn–Teller distortion, which manifest itself by a rather pronounced difference between their values. Moreover, no significant deformations of the MnO_6 units are introduced by the Lu^{3+} doping. This means that the MnO_6 structure is quite independent on the ionic substitution, and consequently, it cannot explain the decrease of cell volume with increasing x.

Figure 5(e) shows the Mn-O1-Mn bond angle value as a function of the Lu^{3+} concentration. The Mn-O1-Mn angle decreases as the dopant concentration increases. From this behavior, an increasing superposition of the Mn-3*d* and O-2*p* electronic orbitals is expected and thus a dominance of the antiferromagnetic to the ferromagnetic interactions.[8–10] This behavior is compatible to the emergence of ferroelectric ground states on the basis of the inverse Dzyaloshinskii–Moriya interaction.[8–10]

As MnO_6 octahedra do not apparently deform with Lu^{3+} doping, the deviation from the ideal cubic structure in orthorhombic $Eu_{1-x}Lu_xMnO_3$ stems almost entirely from changes in the Mn-O1-Mn bond angle.

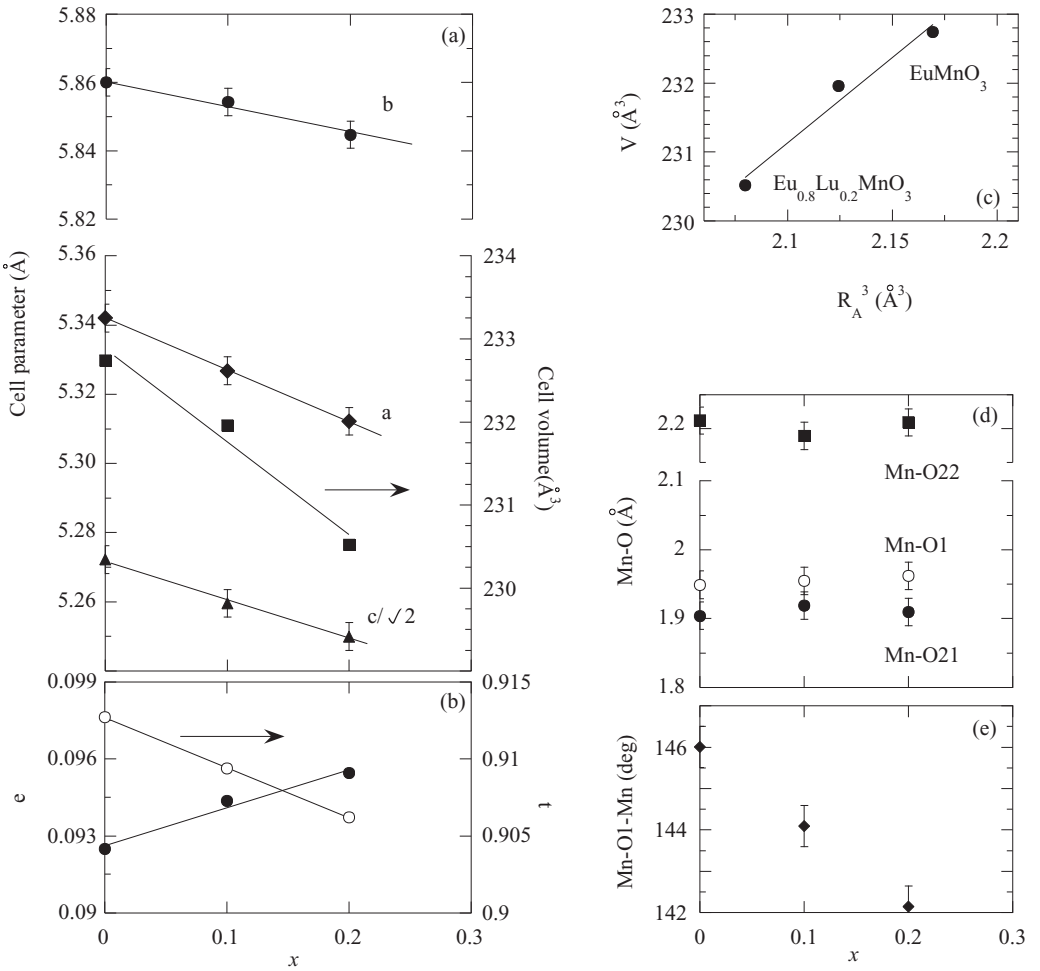

FIG. 5. (a) Lattice parameters and cell volume of $Eu_{1-x}Lu_xMnO_3$ as a function of x. (b) Spontaneous orthorhombic strain e and tolerance factor t as a function of x. (c) Cell volume versus the effective volume of the A site. (d) Mn-O bond lengths and (e) Mn-O1-Mn bond angle as a function of x.

C. Thermodynamic, magnetic, dielectric, and polar characterization

Figures 6(a)–6(c) show the temperature dependence of the ratio M/H, where M stands for the low-field induced magnetization and H the corresponding magnetic field strength, for the compositions with $x = 0$, 0.1, and 0.2, respectively. The magnetization data were obtained in zero-field cooling (ZFC curve) and field cooling (FC curve) conditions, measured under an applied dc magnetic field of 40 Oe.

The amplitudes of the M/H ratio for the different compositions are very different, apparently decreasing with increasing Lu^{3+} concentration. This result clearly reveals the antiferromagnetic character strengthening as x increases.

The shape of the M/H curves enables gathering the various compositions into two main single sets. The first is formed by the $EuMnO_3$ [see Fig. 6(a)], and it is characterized by the existence of a ferromagnetic component at low temperatures, suggested from the increase of the magnetization measured in zero-field cooling conditions, and from the large increase of the magnetization measured in field cooling conditions. As it was referred, this magnetization emerges due to spin canting, which is characteristic of the canted A-type antiferromagnetism.[18–20]

The second single set, comprising the composition with $x = 0.2$ [see Fig. 6(c)] shows a distinct behavior of the induced magnetization. As the magnetic order occurs, the M/H curve gradually decreases with decreasing temperature, for both zero-field and field cooling conditions. This composition can thus be thought as an antiferromagnetic compound.

The intermediate composition $x = 0.1$ is of a mixed nature [see Fig. 6(b)]. The M/H curve measured in zero-field cooling conditions reveals antiferromagnetic character. However, it is still possible to induce a weak magnetization, as it is apparent from the increase at low temperatures of the ferromagnetic component measured in field cooling conditions. This peculiar mixed magnetic behavior reveals that this composition has a distinct place in the (x, T) phase diagram.

Above 60 K, both ZFC and FC curves merge. Just above that temperature, the H/M curve, standing for the inverse of the magnetic susceptibility in the paramagnetic phase, departs from a linear behavior, which is likely associated with short-range magnetic interactions. Moreover, above 100 K, the H/M curve does not follow the Curie–Weiss law due to the van Vleck contribution arising from the low-lying multiplets of Eu^{3+}.[34]

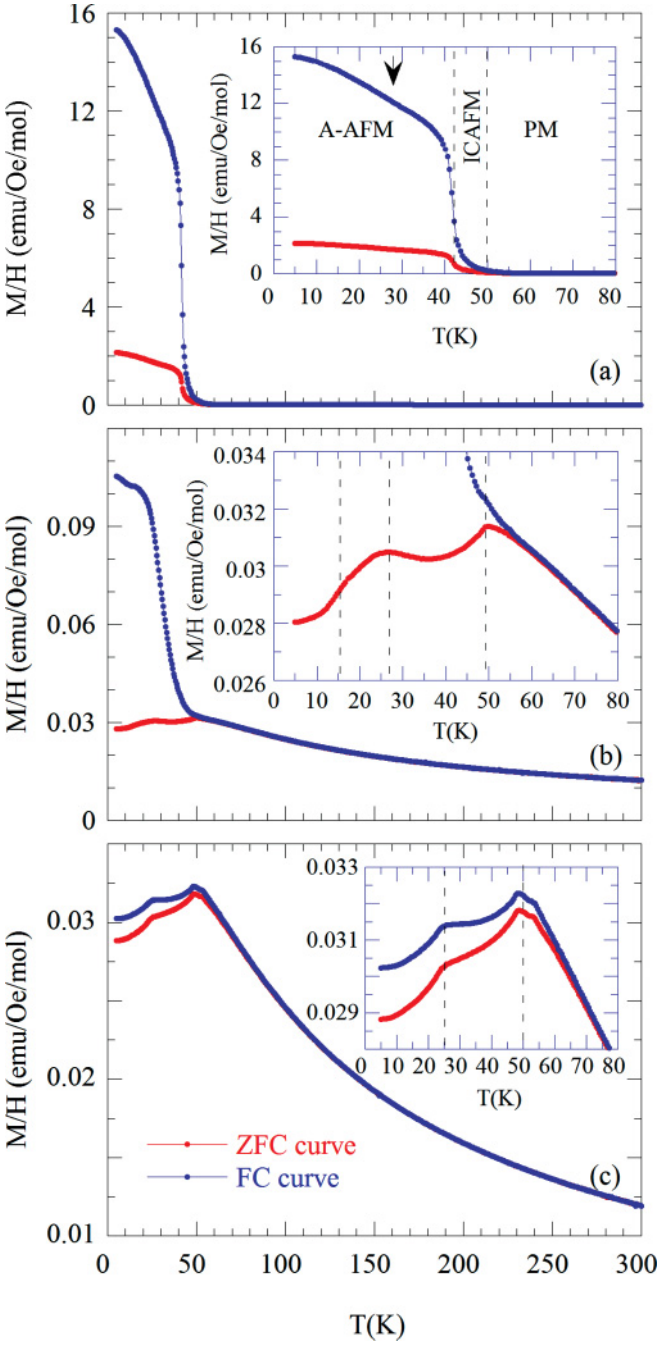

FIG. 6. (Color online) Temperature dependence of the ratio M/H for the compositions with (a) $x = 0$, (b) 0.1, and (c) 0.2. The magnetization data were obtained in zero-field cooling (ZFC curve) and field cooling (FC curve) conditions, measured under an applied dc magnetic field of 40 Oe.

For a detailed analysis of the results above 100 K, we have fitted the following expression to the experimental data:

$$\chi = \frac{C}{T-\theta} + \chi_{VV}(1-x), \tag{4}$$

where the first part corresponds to a Curie–Weiss behavior, and the second to a sum of Eu^{3+} van Vleck-type contributions, emerging from Eu^{3+} low-lying multiplets.[17] Table I presents the parameters obtained from the fit of Eq. (4) to the experimental data above 100 K. The Curie–Weiss constant, the van Vleck susceptibility, and the Curie temperature decrease monotonously as the Lu-content increases. The decrease of van Vleck contribution to the magnetic susceptibility is in good agreement with the decrease of Eu^{3+} concentration. From the Curie–Weiss constant, we calculated the effective paramagnetic moment, whose x dependence is shown in Fig. 7. Taking into account the total spin quantum number $S = 2$ for Mn^{3+} ions, the expected contribution of the Mn^{3+} ions for the total effective paramagnetic moment is 4.9 μ_B. The difference between this value and those presented in Fig. 7 comes apparently from the contribution of the rare-earth ion. This assumption is supported by the decrease of the effective paramagnetic moment as the Eu^{3+} content decreases.

TABLE I. Curie–Weiss constant (C), van Vleck contribution to the magnetic susceptibility (χ_{vv}), and Curie temperature (Θ_c) obtained from the best fit of Eq. (4) to the H/M curves above 100 K.

x	C (K)	χ_{vv}	Θ (K)
0	5.04 ± 0.02	0.00153 ± 0.00003	−80.2 ± 0.7
0.1	4.27 ± 0.02	0.00149 ± 0.00004	−79.5 ± 0.7
0.2	4.037 ± 0.008	0.00137 ± 0.00001	−73.4 ± 0.2

Let us now focus on the temperature behavior of the M/H ratio below 60 K (see Fig. 6). All compositions transform to the AFM-1 phase at T_N that is slightly dependent on x. For the composition with $x = 0$, the T_N value could be ascertained by determining the temperature wherein the ZFC and FC curves start to merge into one another, while for the other compositions, the value of T_N is well signalized by the anomaly of the M/H ZFC curve.

Other phase transitions are well observed for all compositions. For the composition with $x = 0$, the AFM-1 phase is followed by the canted A-type antiferromagnetic phase, which is stable below $T_1 = 43$ K, as it was reported in the early literature.[18–20] For the compositions with $x = 0.1$ and 0.2, the ZFC curve exhibits anomalous behavior at $T_1 = 27$ and 24 K, respectively, giving evidence for the existence of another magnetic phase transition into an AFM-2 phase in both compositions. Moreover, the ZFC curve obtained from the composition with $x = 0.1$ exhibits a small but clear anomaly at around $T_2 = 16$ K, marking a transition into another

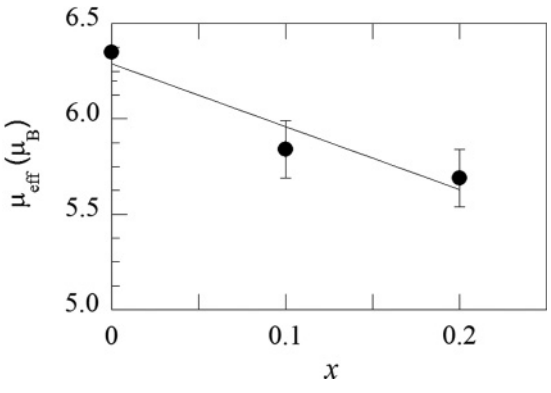

FIG. 7. Effective paramagnetic moment as a function of x.

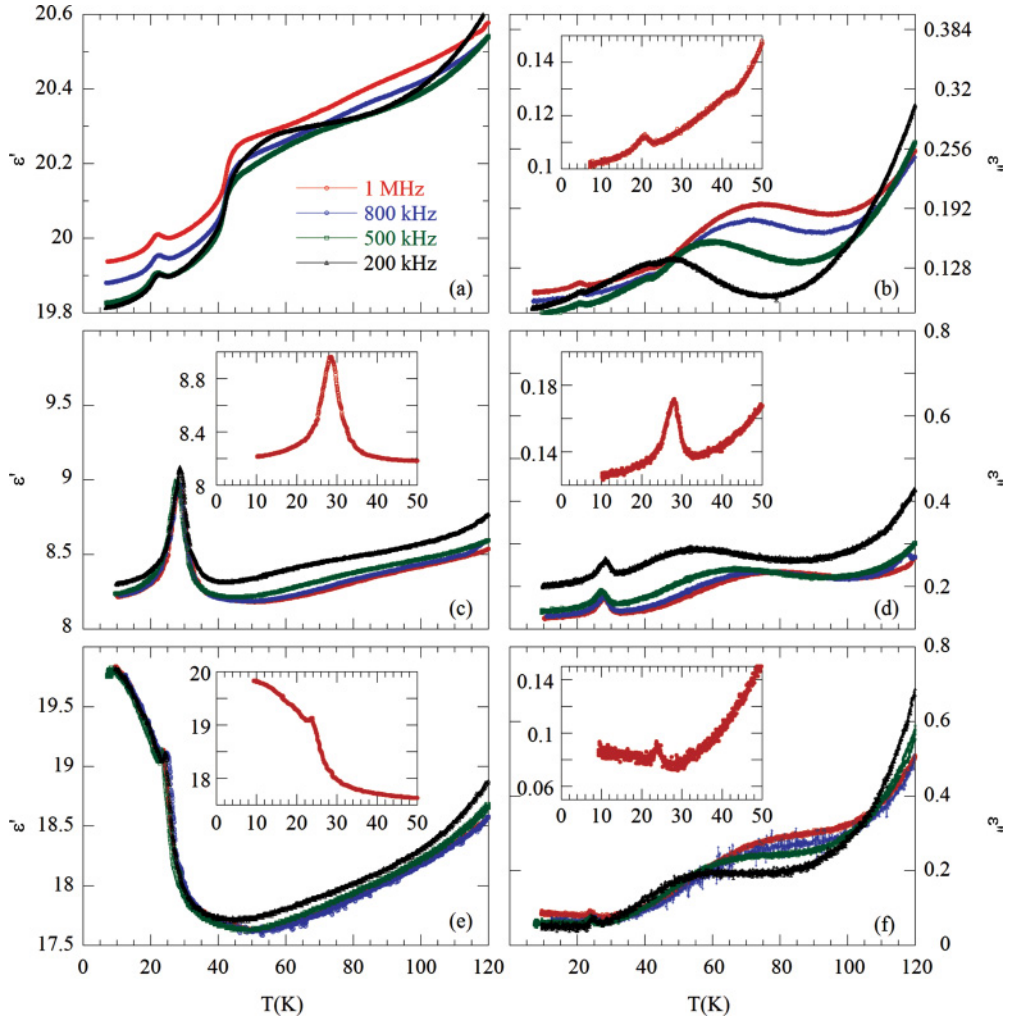

FIG. 8. (Color online) Temperature dependence of both real (ε') and imaginary (ε'') parts of the complex dielectric constant, measured in heating run at several fixed frequencies, for (a) and (b) $EuMnO_3$, (c) and (d) $Eu_{0.9}Lu_{0.1}MnO_3$, and (e) and (f) $Eu_{0.8}Lu_{0.2}MnO_3$. Insets: details of the temperature dependence of ε' and ε'' measured in heating run at 1 MHz.

antiferromagnetic phase, hereafter designated by AFM-3. The characteristic of the antiferromagnetic phases will be discussed later.

Figure 8 shows the temperature dependence of the real (ε') and imaginary (ε'') parts of the complex dielectric constant, measured in heating run at several fixed frequencies in the 1 kHz to 1 MHz frequency range for the different Lu^{3+} concentrations. As it can be deduced from the observation of Fig. 8, the temperature behavior of both ε' and ε'' at a fixed frequency is also strongly dependent of the Lu^{3+} concentration.

For all compositions, the transition into the AFM-1 phase cannot be determined directly from the curves $\varepsilon'(T)$ and $\varepsilon''(T)$, as they do not present any anomaly close to T_N.

The temperature dependence of ε' of $EuMnO_3$ [see Fig. 8(a)] exhibits a step-like anomaly at $T_1 = 43$ K, marking the transition from the AFM-1 phase into the canted A-type antiferromagnetic one.[18–20] The $\varepsilon'(T)$ curve presented, as well as the amplitude of the step ($\Delta\varepsilon \approx 0.3$) are qualitatively similar to the $\varepsilon'(T)$ measured along the a axis in single crystals (ε'_a).[11] Another anomaly at $T' = 23$ K is observed. An anomaly is also observed in the $\varepsilon''(T)$ curve [see Fig. 8(b)], and in $\varepsilon''_a(T)$ of single crystals at the same temperature.[11] A detailed inspection of the temperature dependence of the M/H curves, measured in both zero-field and field cooling conditions, reveals a local tiny minimum at T' and a change of slope of the M/H curve. The anomaly observed in both $\varepsilon'(T)$ and $\varepsilon''(T)$ curves are likely associated with a rearrangement of the spin structure. The increase of the temperature rate of M/H just below T' enables one to conclude that the ferromagnetic interactions are reinforced below $T' = 23$ K.

Figures 8(c) and 8(d) show the temperature dependence of ε' and ε'' for the composition $x = 0.1$. Dramatic changes in shape and amplitude regarding the ones for $x = 0$ are obvious. A well-defined anomaly is detected at $T_1 = 27$ K in both $\varepsilon'(T)$ and $\varepsilon''(T)$, marking the transition into the AFM-2 phase. It is worth stressing that the $\varepsilon''(T)$ anomaly is slightly asymmetric. An enlarged view of the curve $\varepsilon''(T)$ in the temperature range between 10 and 50 K allows us to detect [see detail in Fig. 8(d)] a small anomaly at $T_2 = 16$ K. The existence

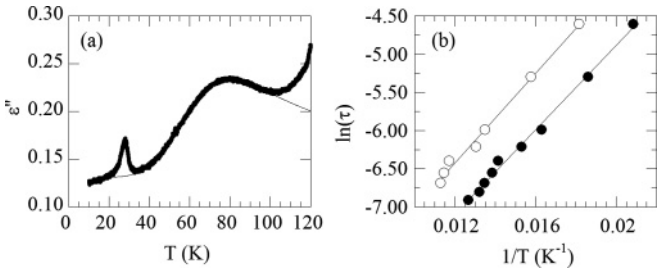

FIG. 9. (a) Best fitting of Eq. (5) to the imaginary (ε'') part of the complex dielectric constant for $Eu_{0.9}Lu_{0.1}MnO_3$ (solid line). (b) Relaxation time as a function of $1/T$ for $Eu_{0.9}Lu_{0.1}MnO_3$ (closed circles) and $Eu_{0.8}Lu_{0.2}MnO_3$ (open circles).

of this anomaly is compatible with another phase transition in this compound, as it was inferred from the magnetic results.

For the composition with $x = 0.2$, $\varepsilon'(T)$ and $\varepsilon''(T)$ show an anomaly at $T_1 = 24$ K [see Figs. 8(e) and 8(f)]. This anomaly is followed by an increase of $\varepsilon'(T)$ as the temperature decreases.

Above 50 K, $\varepsilon''(T)$ curves exhibit a broad anomaly, whose maximum position is strongly dependent on the frequency, which is correlated with relaxation processes not associated with the critical phenomena taking place at lower temperatures. The relaxation behavior in the compounds with $x = 0.1$ and 0.2 was studied by fitting $\varepsilon''(T)$ with the Debye model with a relaxation time obeying the Arrhenius law:[35]

$$\varepsilon''(T) = \frac{\frac{\Delta\varepsilon}{2}}{\cosh\left[\frac{U}{k_B}\left(\frac{1}{T} - \frac{1}{T_M}\right)\right]}, \tag{5}$$

where $\Delta\varepsilon$ is the dielectric strength, U is the activation energy associated with the dielectric relaxation process, k_B is the Boltzmann constant, and T_M is the temperature of the maximum value of $\varepsilon''(T)$. In the fitting procedure, we assumed that the main temperature dependence of $\varepsilon''(T)$ defined by Eq. (5) comes from the argument of the hyperbolic function. By the fitting procedure, we determined the T_M value for each frequency. The corresponding relaxation time is the inverse of that frequency. Figure 9(a) shows an example of the fitting result for the composition $x = 0.1$. Figure 9(b) shows the logarithm of the relaxation time τ as a function of the inverse of temperature for both compositions $x = 0.1$ and 0.2. A linear relation between $\ln(\tau)$ and $1/T$ is found in the temperature range 50 to 90 K, corresponding to the paramagnetic phase. The value of the activation energy is 24 meV, independent of the Lu^{3+} concentration. The aforesaid value is about 25% higher that the corresponding value obtained in the same temperature range in $EuMnO_3$.[17]

Figures 10(a) and 10(b) show the temperature dependence of the specific heat divided by temperature, C/T, for the

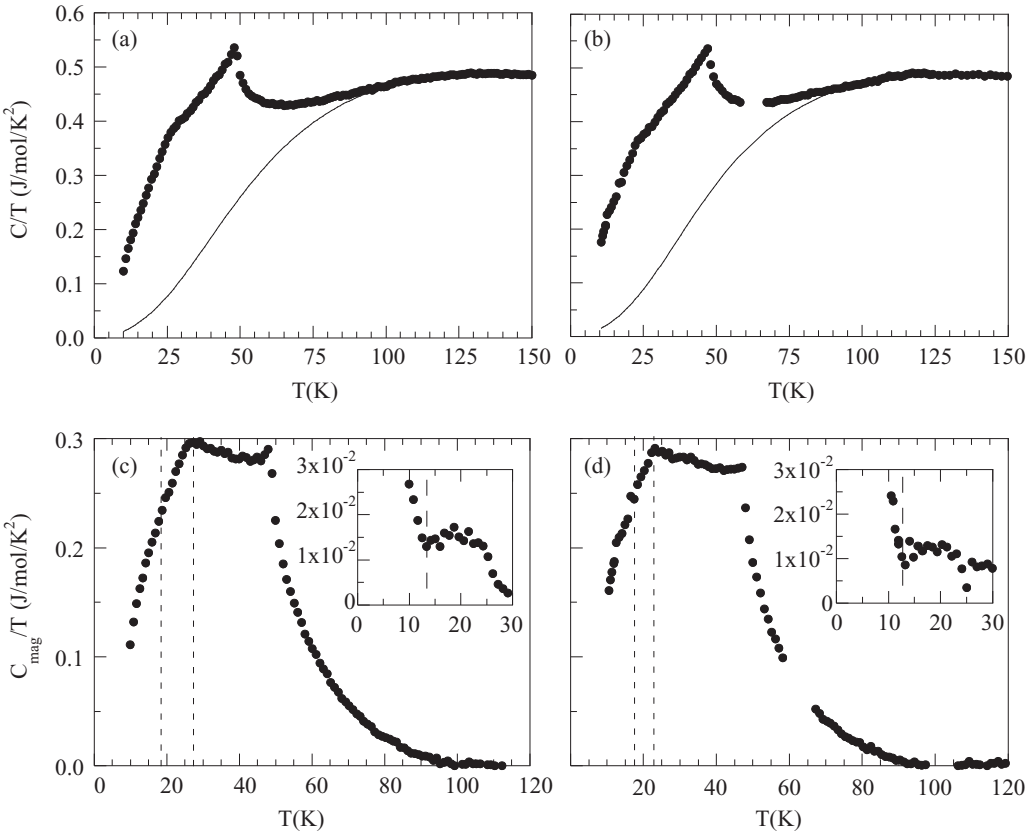

FIG. 10. Temperature dependence of the specific heat divided by temperature measured in heating run for (a) $Eu_{0.9}Lu_{0.1}MnO_3$ and (b) $Eu_{0.8}Lu_{0.2}MnO_3$. Solid lines stand for the best fits of Eq. (6) to the experimental data above 100 K. Temperature dependence of the magnetic contribution to the specific heat divided by temperature calculated from the difference between the experimental curve C/T and the curve obtained from the best fit of Eq. (6) to the experimental data above 100 K for (c) $Eu_{0.9}Lu_{0.1}MnO_3$ and (d) $Eu_{0.8}Lu_{0.2}MnO_3$. Insets: temperature derivative of the C_{mag}/T curve.

compositions $x = 0.1$ and 0.2, respectively, in the temperature range 0–150 K. The C/T data from 100 to 300 K were analyzed by fitting the Debye equation, associated with the lattice contribution, to the specific heat:[36]

$$C_p = N_h\left(\frac{T}{\theta_h}\right)\int_0^{T/\theta_h}\frac{x^4e^x}{(e^x-1)^2}dx + N_l\left(\frac{T}{\theta_l}\right)\int_0^{T/\theta_l}\frac{x^4e^x}{(e^x-1)^2}dx, \quad (6)$$

where N_h and N_l are the number of heavy (Mn, Eu/Lu) and light (O) atoms in the formula unit, respectively. From the chemical composition of the system, we have $N_h = 2$ and $N_l = 3$. The θ_h and θ_l stands for the Debye temperatures for heavy and light atoms, respectively, and are taken as fitting parameters. The solid lines in Figs. 10(a) and 10(b) were obtained from the best fit of Eq. (6) to the C/T data. From the fit procedure, we have determined the values of the Debye temperatures, presented in Table II.

For the compositions $x = 0.1$ and 0.2, the highest temperature anomaly, located at around $T_N = 48$ K, has a lambda-like shape, and it is associated with the transition into the AFM-1 phase. Another anomaly is clearly observed through a change of slope of the C/T curve at $T_1 = 27$ K (for $x = 0.1$) and $T_1 = 23$ K (for $x = 0.2$), marking the transition into the AFM-2 phase. The area between the curve C/T and the fitting curve

TABLE II. Debye temperatures obtained from the best fit of Eq. (6) to the C/T data shown in Fig. 11 above 100 K.

x	θ_h (K)	θ_l (K)
0.1	336	660
0.2	317	674

refers to the magnetic contribution to the specific heat, which enables us to calculate the corresponding entropy contribution:

$$\Delta S = \int_0^{T_M}\frac{C}{T}dT, \quad (7)$$

where T_M is the maximum registered temperature. The mean value of the entropy variation obtained in this way is 13.7 J mol^{-1} K^{-1}. Taking into account that the Mn^{3+} has S = 2, the expected value of the entropy variation ($\Delta S = 13.4$ J K^{-1} mol^{-1}) is in excellent agreement with the experimental value. Figures 10(c) and 10(d) show the magnetic contribution to the specific heat (C_{mag}) divided by temperature, as a function of temperature for the compositions with $x = 0.1$ and 0.2, respectively. This magnetic contribution was calculated from the difference between the experimental specific heat and the Debye curve obtained from the best fit of Eq. (6). The insets shown in Figs. 10(c) and 10(d) depict the temperature dependence of the temperature derivative of C_{mag}/T curves, in the 10–30 K temperature range. The magnetic contribution

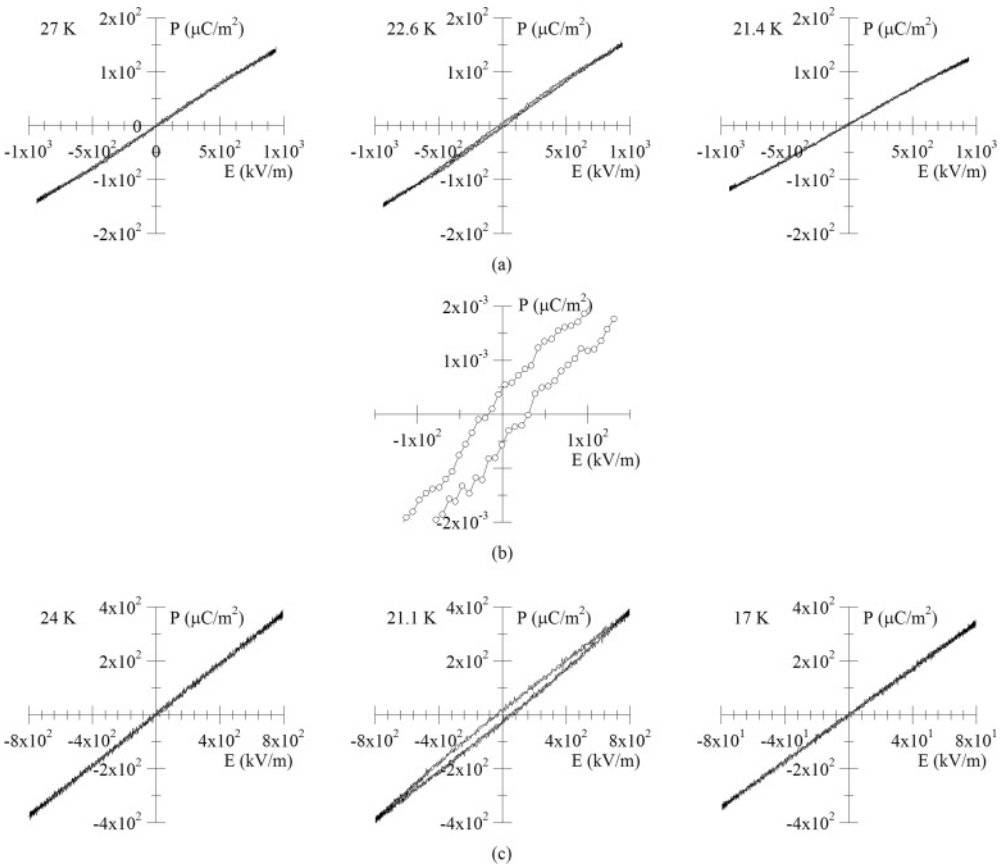

FIG. 11. (a) $P(E)$ relations obtained at several fixed temperatures for $Eu_{0.9}Lu_{0.1}MnO_3$. (b) Expanded view of the $P(E)$ relation recorded at 22.6 K for $Eu_{0.9}Lu_{0.1}MnO_3$. (c) $P(E)$ relations obtained at several fixed temperatures for $Eu_{0.8}Lu_{0.2}MnO_3$.

to the specific heat starts to increase just below 90 K, well above T_N. This result is compatible with the appearance of short-range magnetic interactions above T_N, as it has been observed in other rare-earth manganites. At low temperatures, the magnetic contribution to the specific heat is larger than the one coming from the lattice, in good agreement with the rather high values of the Debye temperatures obtained from the aforesaid fit procedure (see Table II). In both compounds, the transitions into the AFM-1 and into the AFM-2 phases are well marked by an expressive anomaly of C_{mag}/T curve at T_N and at T_1, respectively. The temperature derivative of the C_{mag}/T curve reveals a hint of anomalous temperature behavior at $T_2 = 13$ K (for $x = 0.1$) and at $T_2 = 12$ K (for $x = 0.2$), which is compatible with the existence of another magnetic phase transition. Later in the discussion of the results of the polarization, we will refer to this transition.

In order to fully characterize the ferroelectric properties of this system, we have performed polarization reversal measurements. For the composition $x = 0$, only linear $P(E)$ relations were obtained in the temperature range 8–50 K. This result shows that no polar domain reversal exists in this range of temperatures, confirming that this composition is not ferroelectric, as it was reported earlier.[18–20]

The ac electric field dependence of the electric polarization, $P(E)$, is presented in Fig. 11, for the compositions $x = 0.1$ and 0.2. We start analyzing the results obtained in the composition with $x = 0.1$ [see Fig. 11(a)]. As the temperature decreases from high temperatures towards $T_1 = 26$ K, only linear $P(E)$ relations can be observed. Just above to T_1, S-shaped $P(E)$ curves start to be observed, and on further cooling hysteresis loops are detected from $T_1 = 26$ K to $T_2 = 20$ K, though with an elongated shape. An expanded view of the $P(E)$ relation at 22.6 K is shown in Fig. 11(b). On further cooling, the S-shaped $P(E)$ curves are again retrieved, and for low enough temperatures only linear $P(E)$ relations were observed. For the composition $x = 0.2$ [see Fig. 11(c)], hysteresis loops appears just between $T_1 = 22$ K and $T_2 = 18$ K. As for $x = 0.1$, the $P(E)$ relations exhibit an unusual elongated shaped, as it has been observed in other magnetoelectric manganites.[25,37] This feature is a consequence of the high polarizability of the samples, which is x dependent. The value of the remanent polarization is rather small, although its maximum value increases with x. In fact, the maximum remanent polarization of $Eu_{0.9}Lu_{0.1}MnO_3$ compound ($Pr = 5\ \mu C/m^2$) is about 75% lower than the one in $Eu_{0.8}Lu_{0.2}MnO_3$ compound ($Pr = 34\ \mu C/m^2$). The rather low value of the remanent polarizations points out an improper character of the ferroelectric phase in these compounds. The disappearance of hysteretic $P(E)$ relation below T_2 in both compounds gives strong evidence for the existence of the antiferromagnetic phase AFM-3, stable below T_2, whose spin arrangements do not allow for ferroelectricity.

D. Magnetodielectric properties

Figures 12(a) and 12(b) show the real part of the dielectric constant as a function of the magnetic field ranging from −15 up to 15 T, for the compositions $x = 0.1$ and 0.2, respectively. Dielectric constant was measured at 100 kHz and for several selected temperatures.

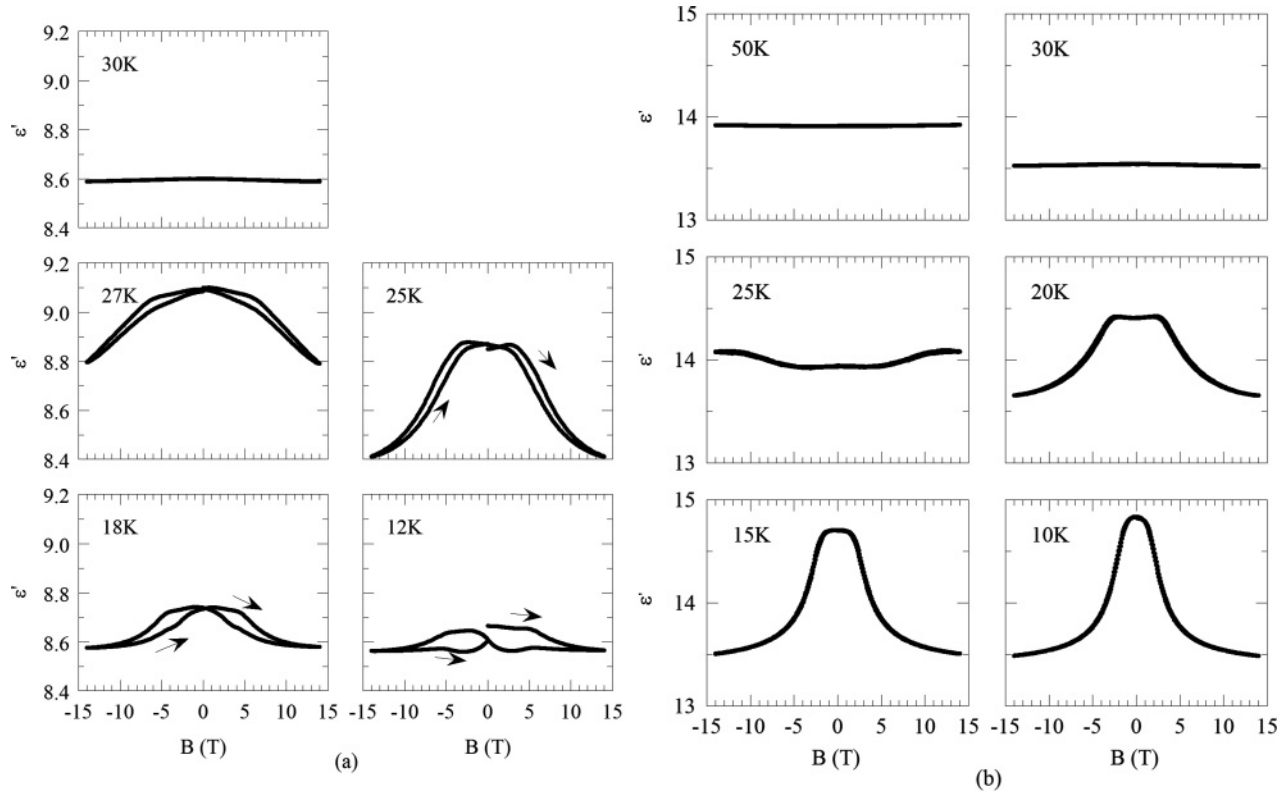

FIG. 12. Magnetic field dependence of the real part of the dielectric constant of (a) $Eu_{0.9}Lu_{0.1}MnO_3$ and (b) $Eu_{0.8}Lu_{0.2}MnO_3$ measured at 100 kHz, at several selected temperatures.

We start presenting the results concerning the composition x = 0.1, which are shown in Fig. 12(a). Well above $T_1 = 26$ K, the effect of the magnetic field on the dielectric constant is negligible. As the temperature decreases towards $T_1 = 26$ K, a nonlinear dependence on the magnetic field starts to be observed in the AFM-2 phase, along with a small magnetic hysteresis. At 27 and 25 K, ε' decreases with increasing magnetic field strength, but the magnetic field induced changes on ε' attains the largest value at 25 K, which is about −5%. In the AFM-3 phase, the shape of $\varepsilon'(B)$ changes, and the magnetic hysteresis increases significantly.

The results obtained for the composition with $x = 0.2$, shown in Fig. 12(b), evidence no significant changes in the magnetic field dependence of ε' in both paramagnetic and AFM-1 phases. At 25 K, just above T_2, small changes in the profile of $\varepsilon'(B)$ start to be observed. While $\varepsilon'(B)$ is quite independent on the magnetic field strength below to 5 T, for higher magnetic field strength ε' increases just up to 10 T, then keeping constant values. In the AFM-2 phase, which is also ferroelectric, the magnetic field dependence of ε' changes dramatically. In fact, at 20 K, ε' exhibits a plateau for $|B| \leqslant 4$ T, and then ε' decreases for higher magnetic field strengths. The amplitude of the magnetic field induced variation in ε' is about −6%. As the temperature decreases, the magnetic field range, where the aforesaid plateau in the $\varepsilon'(B)$ curve is observed, decreases monotonously, and the magnetic field induced variation in ε' increases, reaching −9% at 10 K. The aforementioned magnetic field induced variations in $\varepsilon'(B)$ are rather small, pointing out a small magnetodielectric coefficient. Moreover, the magnetic field effect in ε' is symmetric under the transformation $B \rightarrow -B$, which stands for a quadratic magnetodielectric coupling in this compound with negligible magnetic hysteresis.

IV. CONCLUSIONS

This work presents an experimental study of the physical properties of the system $Eu_{1-x}Lu_xMnO_3$, with $0 \leqslant x \leqslant 0.2$, in order to characterize the system and thus enabling to trace its (x,T) phase diagram, which is presented in Fig. 13.

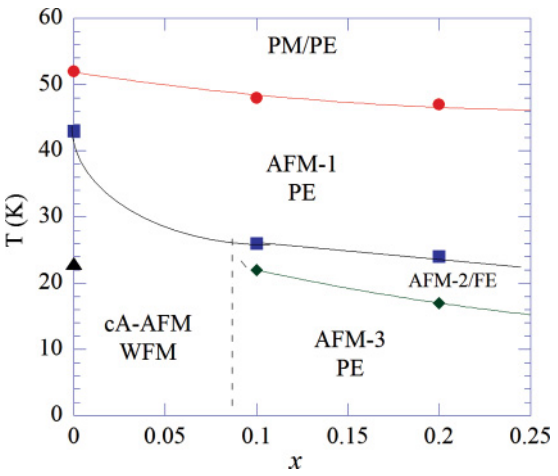

FIG. 13. (Color online) (x, T) phase diagram of the $Eu_{1-x}Lu_xMnO_3$ system, for $0 \leqslant x \leqslant 0.2$.

According to the specific heat and magnetic data, all compositions undergo the first phase transition at $T_N \approx 48$ K. The magnetic structure of the $Eu_{1-x}Lu_xMnO_3$ cannot be experimentally determined by neutron scattering, as the ^{153}Eu has a rather large absorption cross section. So, the magnetic arrangement must be inferred from the macroscopic characterization and by comparison with other rare-earth manganites. In $EuMnO_3$, the spin structure of the AFM-1 has been assigned to an incommensurate sinusoidal and collinear arrangement. We assume that this is the spin arrangement of the AFM-1 for the other compositions.

For $x < 0.1$, a weak ferromagnetic phase seems to develop below T_1 with a canted A-type antiferromagnetic order (cA-AFM). Due to its collinear structure, this phase is not ferroelectric.

For $0.1 \leqslant x \leqslant 0.2$, the AFM-1 phase is followed by an antiferromagnetic phase AFM-2, which is also ferroelectric. If we assume that polarization comes from microscopic mechanisms described by the inverse Dzyaloshinskii–Moriya interaction, a commensurate cycloidal modulated spin structure is expected in AFM-2 phase. The notable difference between the magnetic properties of compounds $EuMnO_3$ and $Eu_{0.9}Lu_{0.1}MnO_3$ is compatible with the existence of a phase line separating the cA-AFM phase, stable on compounds with low concentration of Lu^{3+} ($x < 0.1$) from the AFM-2 and AFM-3 phases observed for $x = 0.1$. However, the fact that the $Eu_{0.9}Lu_{0.1}MnO_3$ compound presents an induced ferromagnetic component under conditions of field cooling suggests that this compound is close to this phase boundary.

The disappearance of hysteretic cycles $P(E)$ below T_2 clearly indicate the existence of the antiferromagnetic phase AFM-3, whose spin structure is not compatible with both the ferroelectric and ferromagnetic component. The spin arrangement can be likely collinear in order to prevent ferroelectricity through the Dzyaloshinskii–Moriya interaction.

The magnetic effect on the dielectric constant revealed the existence of magnetodielectric coupling in the AFM-2 and AFM-3 phases of both $x = 0.1$ and 0.2 compositions, being more pronounced in the later one. The tiny magnitude of the magnetic induced changes in the dielectric constant for both compounds reveals small magnetodielectric coefficient. Conversely to the composition with $x = 0.1$, the composition with $x = 0.2$ does not reveal any significant magnetic hysteresis, which is in favor for the existence of a quadratic magnetodielectric coupling in this compound.

Finally, it was clearly shown that the decrease of the Mn-O1-Mn bond angle plays a paramount role in the deviation of the crystal structure from that of ideal cubic perovskite. According to the theoretical results,[10] the decrease of Mn-O1-Mn bond angle enhances the antiferromagnetic interactions against the ferromagnetic ones, which leads to the (x, T) phase diagram of orthorhombic $Eu_{1-x}Lu_xMnO_3$.

ACKNOWLEDGMENTS

This work was supported by Fundação para a Ciência e Tecnologia through the Project PTDC/CTM/67575/2006 and by Programa Pessoa through Program PHC PESSOA 2011-Ab5356.

*jamoreir@fc.up.pt

[1] T. Choi, Y. Horibe, H. T. Yi, Y. J. Choi, W. Wu, and S. W. Cheong, Nat. Mater. **9**, 253 (2010).

[2] S. Lee, A. Pirogov, M. Kang, K. H. Jang, M. Yonemura, T. Kamiyama, S. W. Cheong, F. Gozzo, Namsoo Shin, H. Kimura, Y. Noda, and J. G. Park, Nature **451**, 805 (2008).

[3] M. Gajek, M. Bibes, S. Fusil, K. Bouzehouane, J. Fontcuberta, A. Barthélémy, and Albert Fert, Nat. Mater. **6**, 296 (2007).

[4] W. Eerenstein, N. D. Mathur, and J. F. Scott, Nature **442**, 759 (2006).

[5] T. Goto, Y. Yamasaki, H. Watanabe, T. Kimura, and Y. Tokura, Phys. Rev. B **72**, 220403 (2005).

[6] I. A. Sergienko and E. Dagotto, Phys. Rev. B **73**, 094434 (2006).

[7] Q. Li, S. Dong, and J. M. Liu, Phys. Rev. B **77**, 054442 (2008).

[8] H. Katsura, N. Nagaosa, and A. V. Balatsky, Phys. Rev. Lett. **95**, 057205 (2005).

[9] T. Kimura, S. Ishihara, H. Shintani, T. Arima, K. T. Takahashi, K. Ishizaka, and Y. Tokura, Phys. Rev. B **68**, 060403(R) (2003).

[10] M. Mochizuki and N. Furukawa, Phys. Rev. B **80**, 134416 (2009).

[11] T. Goto, T. Kimura, G. Lawes, A. P. Ramirez, and Y. Tokura, Phys. Rev. Lett. **92**, 257201 (2004).

[12] T. Kimura, G. Lawes, T. Goto, Y. Tokura, and A. P. Ramirez, Phys. Rev. B **71**, 224425 (2005).

[13] N. Kida, Y. Ikebe, Y. Takahashi, J. P. He, Y. Kaneko, Y. Yamasaki, R. Shimano, T. Arima, N. Nagaosa, and Y. Tokura, Phys. Rev. B **78**, 104414 (2008).

[14] J. Strempfer, B. Bohnenbuck, M. Mostovoy, N. Aliouane, D. N. Argyriou, F. Schrettle, J. Hemberger, A. Krimmel, and M. V. Zimmermann, Phys. Rev. B **75**, 212402 (2007).

[15] R. Feyerherm, E. Dudzik, A. U. B. Wolter, S. Valencia, O. Prokhnenko, A. Maljuk, S. Landsgesell, N. Aliouane, L. Bouchenoire, S. Brown, and D. N. Argyriou, Phys. Rev. B **79**, 134426 (2009).

[16] C. Wehrenfennig, D. Meier, Th. Lottermoser, Th. Lonkai, J. U. Hoffmann, N. Aliouane, D. N. Argyriou, and M. Fiebig, Phys. Rev. B **82**, 100414 (2010).

[17] W. S. Ferreira, J. Agostinho Moreira, A. Almeida, M. R. Chaves, J. P. Araújo, J. B. Oliveira, J. M. Machado Da Silva, M. A. Sá, T. M. Mendonça, P. Simeão Carvalho, J. Kreisel, J. L. Ribeiro, L. G. Vieira, P. B. Tavares, and S. Mendonça, Phys. Rev. B **79**, 054303 (2009).

[18] J. Hemberger, F. Schrettle, A. Pimenov, P. Lunkenheimer, V. Y. Ivanov, A. A. Mukhin, A. M. Balbashov, and A. Loidl, Phys. Rev. B **75**, 035118 (2007).

[19] Y. Yamasaki, S. Miyasaka, T. Goto, H. Sagayama, T. Arima, and Y. Tokura, Phys. Rev. B **76**, 184418 (2007).

[20] J. Agostinho Moreira, A. Almeida, W. S. Ferreira, M. R. Chaves, J. B. Oliveira, J. M. Machado da Silva, M. A. Sá, S. M. F. Vilela, P. B. Tavares, Solid State Commun. **151**, 368 (2011).

[21] A. Pimenov, A. Loidl, A. A. Mukhin, V. D. Travkin, V. Yu. Ivanov, and A. M. Balbashov, Phys. Rev. B **77**, 014438 (2008); J. Agostinho Moreira, A. Almeida, W. S. Ferreira, J. E. Araújo, A. M. Pereira, M. R. Chaves, J. Kreisel, S. M. F. Vilela, and P. B. Tavares, *ibid.* **81**, 054447 (2010).

[22] S. Danjoh, J. S. Jung, H. Nakamura, Y. Wakabayashi, and T. Kimura, Phys. Rev. B **80**, 180408 (2009).

[23] J. Agostinho Moreira, A. Almeida, W. S. Ferreira, J. P. Araújo, A. M. Pereira, M. R. Chaves, M. M. R. Costa, V. A. Khomchenko, J. Kreisel, D. Chernyshov, S. M. F. Vilela, and P. B. Tavares, Phys. Rev. B **82**, 094418 (2010).

[24] Y. Takahashi, Y. Yamasaki, N. Kida, Y. Kaneko, T. Arima, R. Shimano, and Y. Tokura, Phys. Rev. B **79**, 214431 (2009).

[25] J Agostinho Moreira, A. Almeida, W. S. Ferreira, M. R. Chaves, B. Kundys, R. Ranjith, W. Prellier, S. M. F. Vilela, and P. B. Tavares, J. Phys. Condens. Matter **21**, 446002 (2009).

[26] H. Murakawa, Y. Onose, F. Kagawa, S. Ishiwata, Y. Kaneko, and Y. Tokura, Phys. Rev. B **80**, 041201(R) (2009).

[27] J. Agostinho Moreira, A. Almeida, W. S. Ferreira, M. R. Chaves, J. B. Oliveira, J. M. Machado da Silva, M.A. Sá, S.M.F. Vilela, and P. B. Tavares, J. Electroceram. **25**, 203 (2010).

[28] J. A. Alonso, M. J. Martínez-Lope, M. T. Casais, and M. T. Fernández-Díaz, Inorg Chem **39**, 917 (2000).

[29] Y. Tadokoroa, Y. J. Shana, T. Nakamuraa, and S. Nakamurab, Solid State Ionics **108**, 261 (1998).

[30] B. B. van Aken, A. Meetsma and T. T. M. Palstra, Acta Cryst. C **57**, 230 (2001).

[31] L. Martín-Carrón, A. de Andrés, M. J. Martínez-Lope, M. T. Casais, and J. A. Alonso, Phys. Rev. B **66**, 174303 (2002).

[32] R. D. Shannon, Acta Cryst. A **32**, 751 (1976).

[33] A. S. Bhalla, R. Guo, and R. Roy, Mat. Res. Innovat. **4**, 3 (2000).

[34] K. H. Buschow and F. R. de Boer, *Physics of Magnetism and Magnetic Materials* (Kluwer Academic/Plenum Publishers, New York, 2003), p. 15.

[35] C. J. F. Böttcher and P. Bordewijk, *Theory of Electric Polarization*, Vol. 2 (Elsievier, New York, 1978), p. 59.

[36] D. G. Tomuta, S. Ramakrishnan, G. J. Niewenhuys, and J. A. Mydosh, J. Phys. Condens. Matter **13**, 4543 (2001).

[37] J. Agostinho Moreira, A. Almeida, W. S. Ferreira, M. R. Chaves, J. P. Araújo, A. M. Pereira, S. M. F. Vilela, and P. B. Tavares, J. Phys. Condens. Matter **22**, 125901 (2010).